The International Journal of Advanced Manufacturing Technology (2019) 101:2051–2064
https://doi.org/10.1007/s00170-018-3089-0

ORIGINAL ARTICLE

Narrow-seam identification and deviation detection in keyhole deep-penetration TIG welding

Baori Zhang [1,2] · Yonghua Shi [1,2] · Shengyong Gu [1,2]

Received: 3 July 2018 / Accepted: 19 November 2018 / Published online: 27 November 2018

Abstract
A narrow-seam identification algorithm is developed to achieve seam tracking in keyhole deep-penetration tungsten inert gas welding (TIG). The welding images are captured by a high-dynamic-range camera and denoised by a bilateral filter based on a noise model analysis. The arc area is extracted as a fixed region of interest. Then, an improved Otsu algorithm and a parabolic fitting algorithm are used to obtain the centerline of the arc. The seam area is extracted as an adaptive region of interest based on a proposed HOG+LBP algorithm. Thereafter, a continuous single-pixel edge contour is extracted by the canny algorithm, and a proposed contour curvature evaluation method is used to obtain the corresponding pixel coordinates. After testing and analysis, the deviation can be reliably detected with an average measurement error within ± 0.04 mm. As a result, the algorithm proposed in this study can accurately identify the deviation during keyhole deep-penetration TIG welding, and has application prospects in the narrow-seam welding field.

Keywords Keyhole deep penetration TIG welding · Narrow seam tracking · Adaptive region of interest · Curvature evaluation method

1 Introduction

Compared with traditional-controlled welding and robot teaching welding, sensor-based seam-tracking welding technology is more stable and efficient in actual welding processes. To achieve seam tracking, visual sensors are commonly used in the field of robot welding to obtain the features of the weld pool and weld edge. For active optical vision, an external auxiliary light source should be projected onto the weldment. Zhang et al. developed a structured light 3D vision system to extract the sag geometry behind the pool [1] and used these features to control the weld fusion via a closed-loop system [2]. Kiddee et al. [3] proposed a weld-seam tracking system using cross mark structured light. Ding et al. [4] proposed a shape-matching algorithm to achieve seam-tracking process that is adaptive to different groove types. Passive optical vision provides more detailed information, including the shapes of the welding arc and groove, and other features, such as the width of the weld pool [5–7]. These methods are suitable for detecting seams with obvious shape features, such as fillet-weld joints, V-grooves, square grooves, etc. However, keyhole deep-penetration TIG welding is butt welding and the weld gap can reach 0.2 mm, which is very narrow, as shown in Fig. 1. The seam is difficult to detect because the laser beam that irradiates onto the weldment is almost not deflected. In addition, the current is relatively high in order to achieve deep-penetration welding and will produce a strong arc light, which greatly interferes with the detection of the laser beam. To solve this problem, high-precision active optical sensors are needed, but the costs are increased due to the high cost of the equipment. GAO et al. [8] proposed an approach to detect the micro-gap weld based on a

---

✉ Yonghua Shi
yhuashi@scut.edu.cn

[1] School of Mechanical and Automotive Engineering, South China University of Technology, Guangzhou 510640, China

[2] Guangdong Provincial Engineering Research Center for Special Welding Technology and Equipment, South China University of Technology, Guangzhou 510640, China

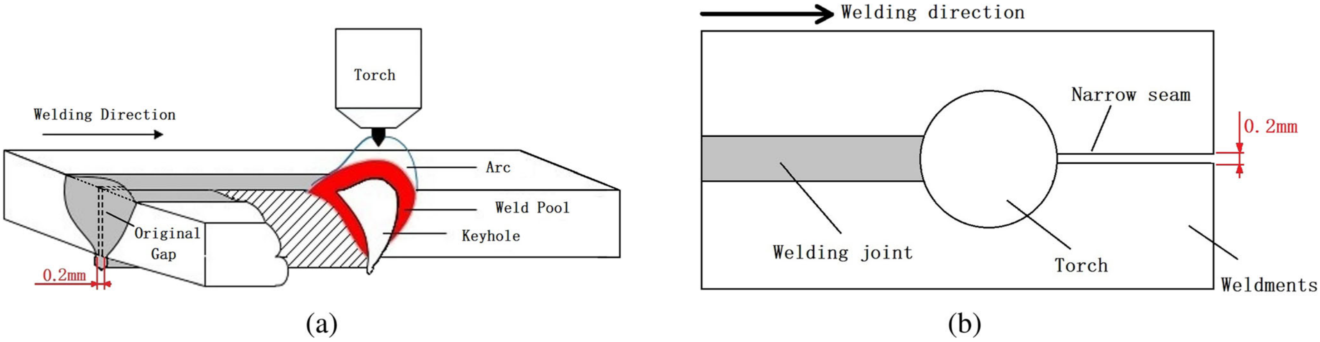

Fig. 1 Schematic diagram of the K-TIG welding process: **a** cross-section of the process; **b** top view of the process

magneto-optical imaging sensor with an excessive size. Yang et al. [9] studied the average method of arc sensing to satisfy the need of seam tracking, but only for narrow gap rotating arc welding.

In this study, passive optical vision sensors are used in keyhole deep-penetration TIG (K-TIG) welding, and the arc produced during welding is used directly as the light source. Images captured by industrial cameras are directly transferred to industrial computers for image processing, and the geometric features of the seam and arc contour are accurately extracted in order to obtain the deviation between the arc centerline and the welding seam coordinate.

2 Welding robot system

The welding system used in this experiment is composed of five parts: a K-TIG welding system, a KUKA robot, a control cabinet, an industrial computer, and a CMOS camera [10, 11].The schematic is shown in Fig. 2. The welding torch is fixed on the KUKA robot end effector and the CMOS camera is fastened on the torch with a fixture. During the welding process, the torch moves along the welding seam, i.e., along the *y*-axis direction of the *O*-*XYZ* coordinates. The installation location and welding direction are shown in Fig. 3. In this study, the welding process produces a strong arc light, which causes the incident light intensity exceeding the upper limit of ordinary industrial camera sensors [12]. The details of the weld-pool image are lost because the photosensitive unit inside the camera achieves light saturation within a short-exposure time. Therefore, an HDR-CMOS camera (NSC1003) is used to capture the image details during the welding process. Afterwards, the regions of interest (ROI) are segregated for feature extraction. The flowchart of the narrow-seam identification process in K-TIG welding is shown in Fig. 4.

Fig. 2 System configuration of the keyhole deep-penetration welding

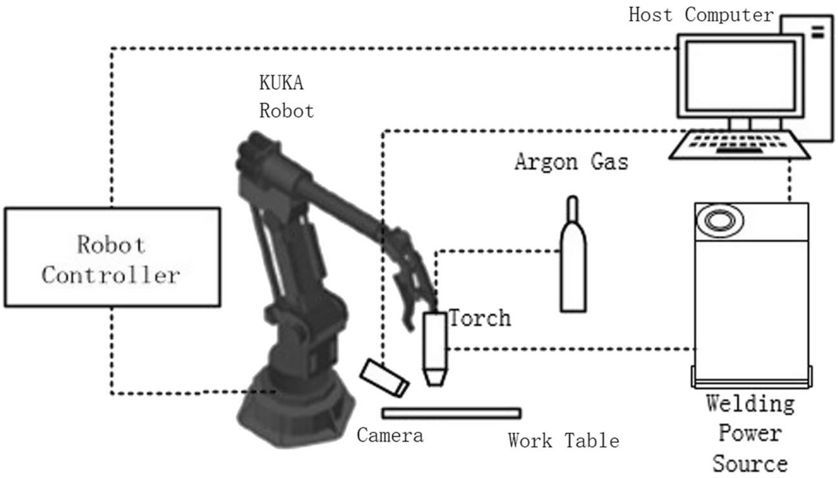

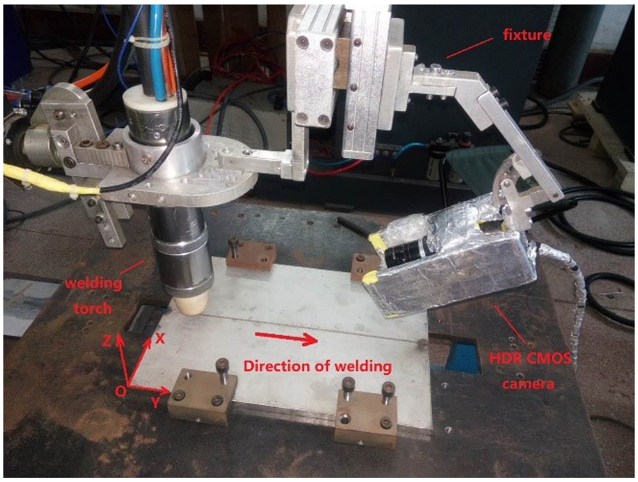

Fig. 3 Torch, camera fixture installation, and welding direction

3 Image denoising

Reflections, splashes, electromagnetic pulses, and other typical environmental influences are produced during the welding process, resulting in blurry images. In many studies, the weld images are denoised before feature extraction on the assumption that the type of noise is known [13, 14]. In this case, the denoising of the image is often very blind because an unmatched denoising algorithm may be wrongly applied to the blurry image. In this study, a method of identifying the noise type in the wavelet domain is used to prevent this problem. According to existing research, after the blurry images are wavelet-transformed, the coefficients of high-frequency subbands vary with different noise types [15]. Moreover, the image noise generated during welding can be mainly divided into Gaussian noise and salt and pepper noise. Therefore, by observing the high-frequency subbands' histograms of welding images, the type of noise can be determined. By analyzing Fig. 5b, the type of noise in the original image can be determined to be Gaussian noise [15]. Therefore, Gaussian filtering is used for denoising, but the edges of the tungsten needle and the weld pool are still blurred (as shown in Fig. 6b). To solve this problem, bilateral filtering that considers spatial information and gray similarity [16] is used instead. As shown in Fig. 6c, by comparison, bilateral filtering can remove noise while preserving the edges.

4 Arc detecting

4.1 Regional binarization

As shown in Fig. 3, the relative position of the CMOS camera and the tungsten needle is fixed so that the tungsten needle always appears in a fixed position in the welding image. As a result, the position of the arc emitted by the tungsten needle is also in a relatively fixed area in the welding image. Therefore, a fixed region of interest (ROI1) can be scheduled in order to accurately extract the characteristics of the arc (as shown in Fig. 7).

The gray values in ROI1 in different frame images changes due to the brightness of the arc, weld-pool reflection, and weldment brightness. The Otsu algorithm [17] is used to automatically obtain the threshold rather than using a fixed threshold for segmentation. Then, mathematical morphology is used for edge smoothness. However, the arc contour feature cannot be effectively obtained if the Otsu algorithm is used directly (as shown in Fig. 8a). An inappropriate threshold selection erroneously considers the background area near the arc as the target area. On the basis of this condition, the traditional Otsu algorithm is improved in a way that the threshold of the original algorithm is multiplied by an appropriate multiple r. When the current threshold is assumed to be T, the improved threshold formula is given as follows:

$$T_r = r \times T \tag{1}$$

As shown in Fig. 8, after the analysis of a large number of experiments, the coefficient $r = 1.4$ is selected and the ideal segmentation effect is obtained. The divided binary image can effectively reflect the shape of the arc. Figure 8e is processed by an edge-pixel search algorithm, and a binary image is obtained containing only the perimeter pixels of the arc (as shown in Fig. 9).

Fig. 4 Flowchart of narrow-seam identification process

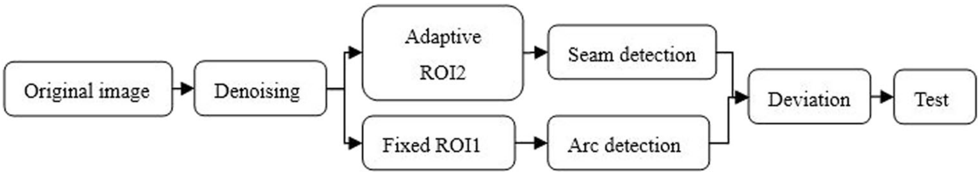

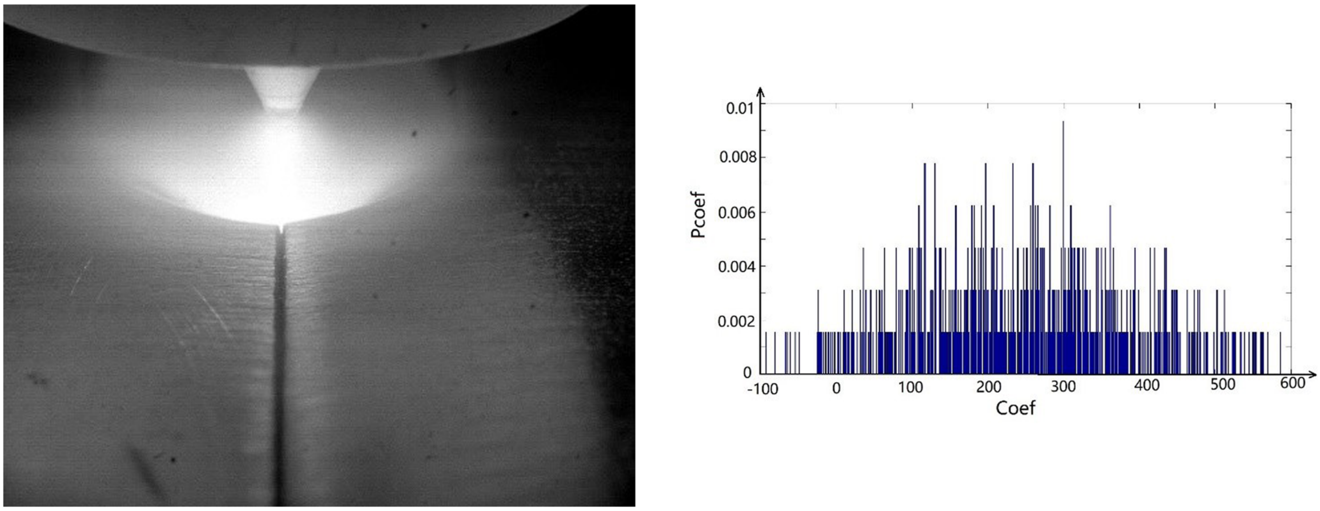

(a) (b)

Fig. 5 Welding image and histograms of the high-frequency subband: **a** welding image captured by CMOS camera; **b** high-frequency subband histogram of **a**

4.2 Arc-edge curve fitting

In the image coordinate system *O-UV*, the arc characteristic is approximated with a parabola via the least-squares method. The coordinates of each discrete point in the image are the pixel coordinates of the contour line. The fitting formula $s(x)$ is expressed as follows:

$$s(x) = a_0 + a_1 x + a_2 x^2 \tag{2}$$

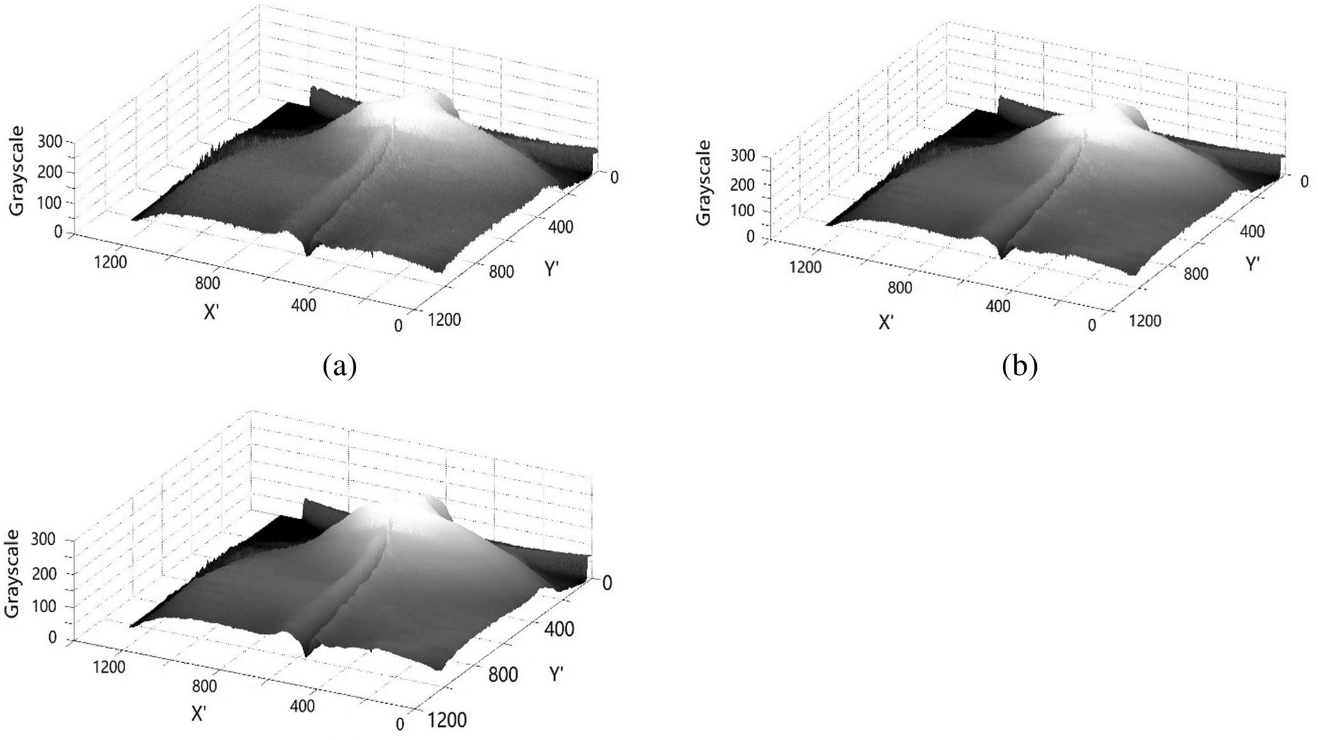

(a) (b)

(c)

Fig. 6 Grayscale stereograms of welding image before and after denoising: **a** welding image; **b** Gaussian-filtered image from (**a**); **c** bilateral-filtered image from (**a**)

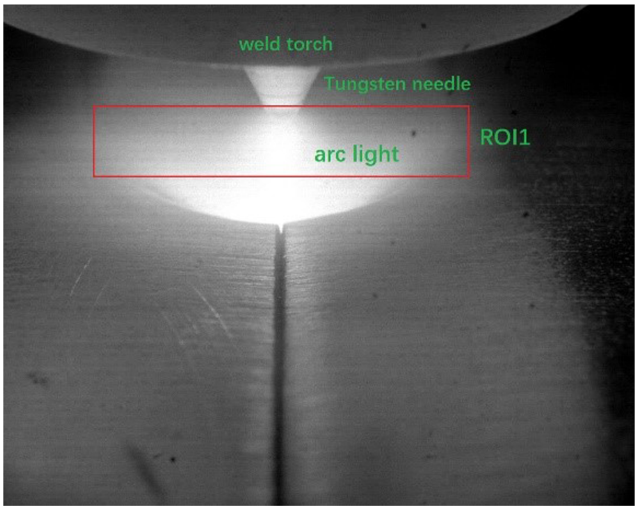

Fig. 7 ROI1 in welding image capture by the CMOS camera

Among the parameters, the pending parameters a_0, a_1, and a_2 are the regression coefficients. Assuming that $f(x)$ is a discrete function of $n+1$, discrete points in the image by detecting the data of the observation points are as follow:

$$(x_j, f(x_j))\ j = 0, 1, 2, \ldots, N. \tag{3}$$

A function $s^*(x)$ is required for the approximate continuous model of the discrete function $f(x)$ and to minimize the sum of squared residuals of $s^*(x)$ and $f(x_j)$ [18, 19]:

$$\delta_i = f(x_i) - s^*(x_i)\quad i = 0, 1, 2, \ldots, n. \tag{4}$$

$$\|\delta\|_2^2 = \sum_{j=0}^{n} \delta_j^2 = \sum_{j=0}^{n} \left[f(x_i) - s^*(x_i)\right]^2$$

$$= \min_{s\in\varnothing} \textstyle\sum_{j=0}^{n} \left[f(x_i) - s^*(x_i)\right]^2 \tag{5}$$

Among the residuals, $\delta = [\delta_0, \delta_1, \ldots \delta_n]^T$ and $\varnothing$ is the specified function space. The fitting parameter values are obtained via the least-squares method, from which the centerline of the arc is obtained. The formula is given as follows:

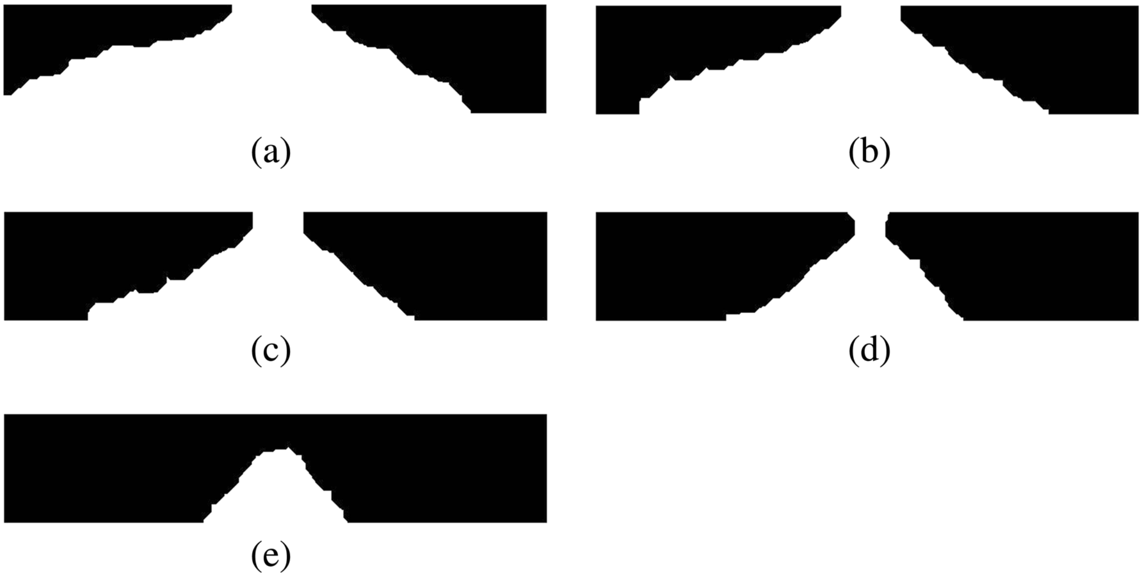

Fig. 8 Arc edge obtained by the Otsu algorithm with different r values: **a** $r = 1$; **b** $r = 1.1$; **c** $r = 1.2$; **d** $r = 1.3$; **e** $r = 1.4$

Fig. 9 Extracted arc contour curve in the image coordinate system *O-UV*

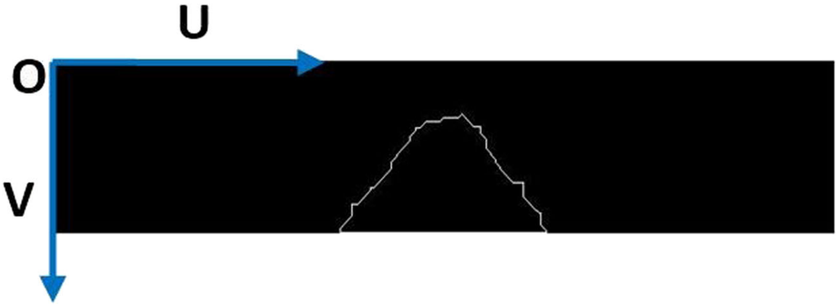

Fig. 10 Midline extracted from the parabolic curve after fitting

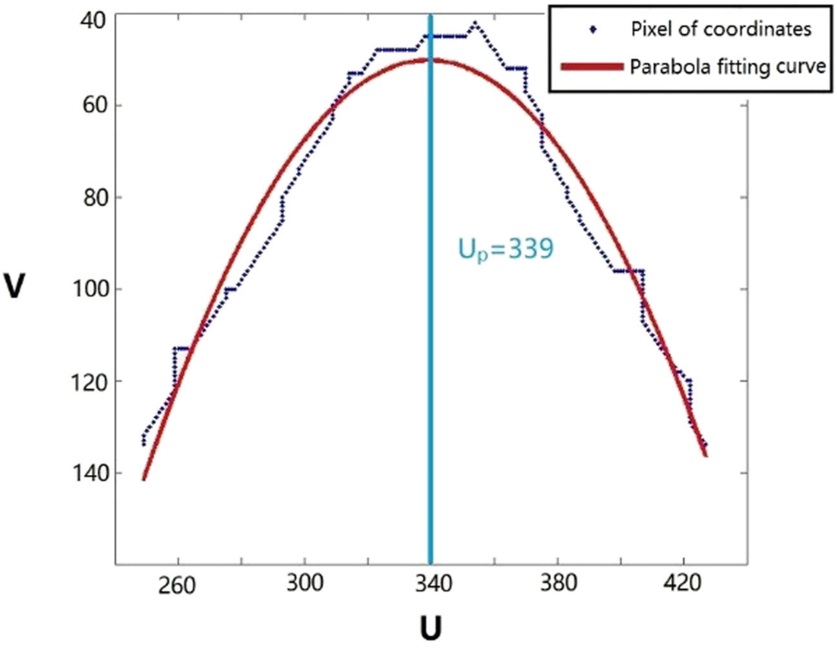

$$U_p = -\frac{a_1}{2a_2} \tag{6}$$

Subsequently, the coordinates of each pixel in Fig. 9 are extracted and saved in the computer memory. The coordinates of each point are indicated by the blue points in Fig. 10. The formula fits these discrete points into a parabola, which exhibits a stable arc shape, as indicated by the red curve in Fig. 10. After parabolic fitting, this method can effectively find the arc centerline, as indicated by the green line in Fig. 11.

5 Identification of the welding seam

During the welding process, it is difficult to obtain the seam features with conventional image processing methods because the seam width is too narrow. In addition, due to the large intensity of the K-TIG welding arc, the grayscale of the image changes in the direction along the seam. In this study, it is determined that in the area where the weld seam meets the weld pool, the molten metal fills in the gap and forms a concave feature that can be used to detect the weld seam. The shapes of the concave feature can be divided into three types according to different seam widths (as shown in Fig. 12). Therefore, the area where the weld seam meets the weld pool can be segmented as the region of interest (ROI2) for the extraction of the weld seam. However, the position of ROI2 will change as the weld seam position changes in the image during the welding process, so it is necessary to use an adaptive ROI2 use rather than a fixed ROI2.

Fig. 11 Extraction of the arc centerline

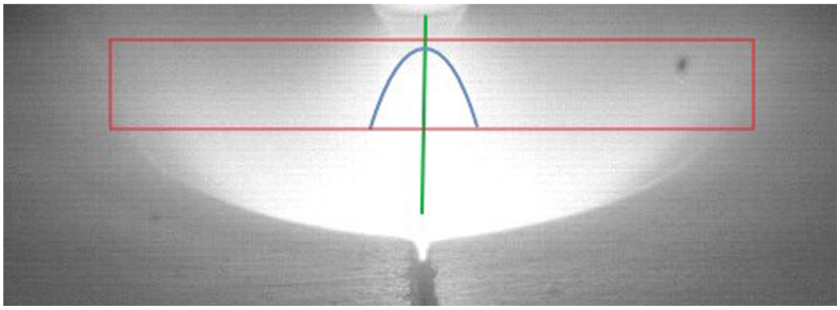

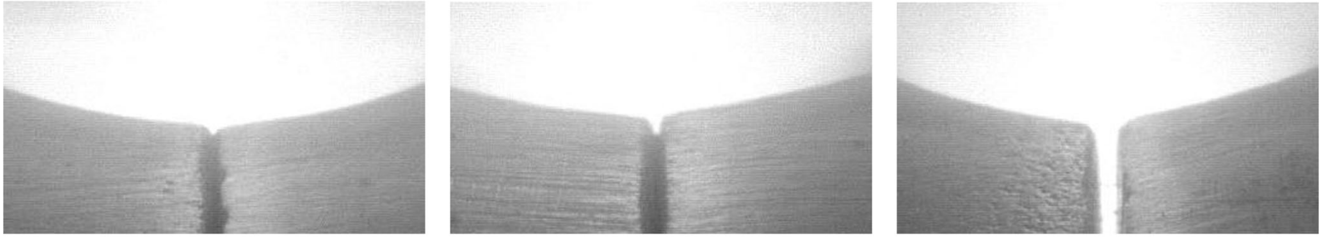

(a) (b) (c)

Fig. 12 Different shapes of the concave feature with various seam widths: **a** small seam width; **b** moderate seam width; **c** large seam width

5.1 SVM training and ROI2 extraction

To obtain ROI2, a segmentation algorithm with an adaptive window is proposed in this study. A fixed-size window (128 × 64) is used to traverse a welding image, obtaining multiple windows of the image corresponding to different locations in the welding image. Then, the image features are extracted from these windows with the feature extraction algorithm. The SVM is used to classify the windows of the images based on these extracted features [20].

First, the SVM needs to be trained by the image samples. Image samples that contain the weld seam and the molten pool are positive samples, while the other samples are negative samples. The numbers of positive and negative samples are 1000 and 1200, respectively, and all the training samples are 128 × 64 in size [21].

Then, the trained SVM is used to obtain ROI2 from new welding images by a similar principle. Several windows are extracted from every new welding image and processed by the feature extraction algorithm. These windows are classified into two categories by the trained SVM. By averaging the position coordinates of the category of windows that contain the intersection of the weld and the weld pool, a new window is obtained, which is the desired ROI2.

5.2 Feature extraction algorithm

To extract ROI2 more accurately, an appropriate feature description algorithm must be selected to extract the image features. HOG and LBP are two commonly used feature descrip-

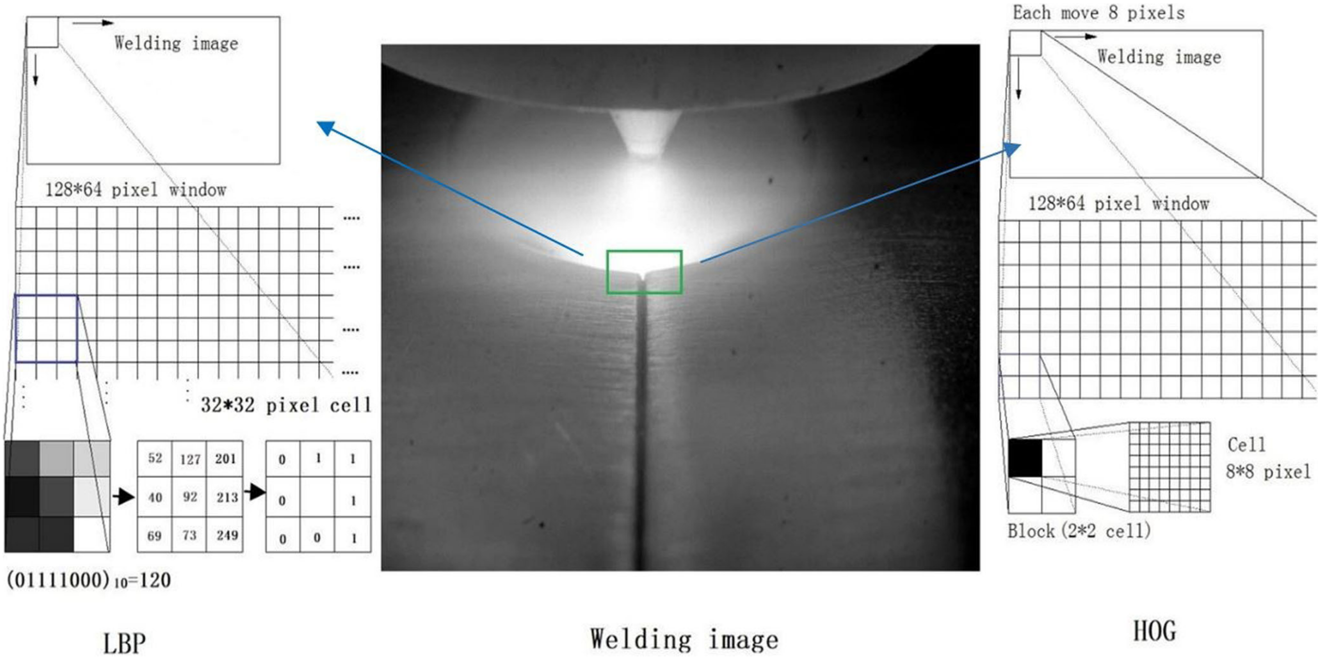

Fig. 13 Principle of the HOG algorithm and LBP algorithm

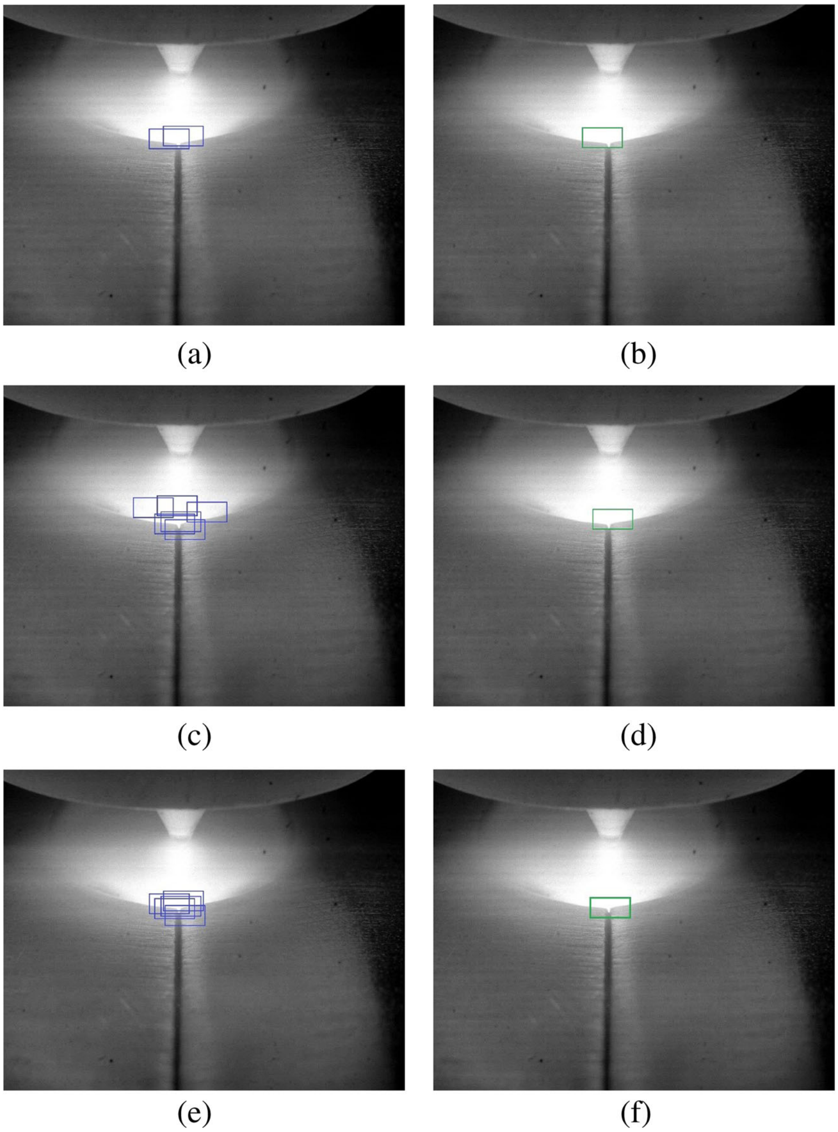

Fig. 14 Testing results: **a** windows extracted by HOG; **b** ROI2 extracted by HOG; **c** windows extracted by LBP; **d** ROI2 extracted by LBP; **e** windows extracted by HOG+LBP; **f** ROI2 extracted by HOG+LBP

tion algorithms. These two algorithms are used separately for testing in this paper.

Histogram of oriented gradient (HOG) can maintain good invariance on both geometric and optical deformations of an image, so it can be used to describe the local features of the windows. The windows with a size of 128 × 64 pixels will be divided into 128 units of 8 × 8 pixels, and then the 2 × 2 area units will be combined into a connecting block for a total of 105 pixel blocks [22] (as shown in Fig. 13). In each cell, the gradient directions of

Table 1 Comparison between HOG, LBP, and HOG+LBP

	HOG	LBP	HOG+LBP
The number of windows identified in 10 images	33	49	51
The number of windows correctly identified	31	40	49
Accuracy	93.93%	81.63%	96.07%

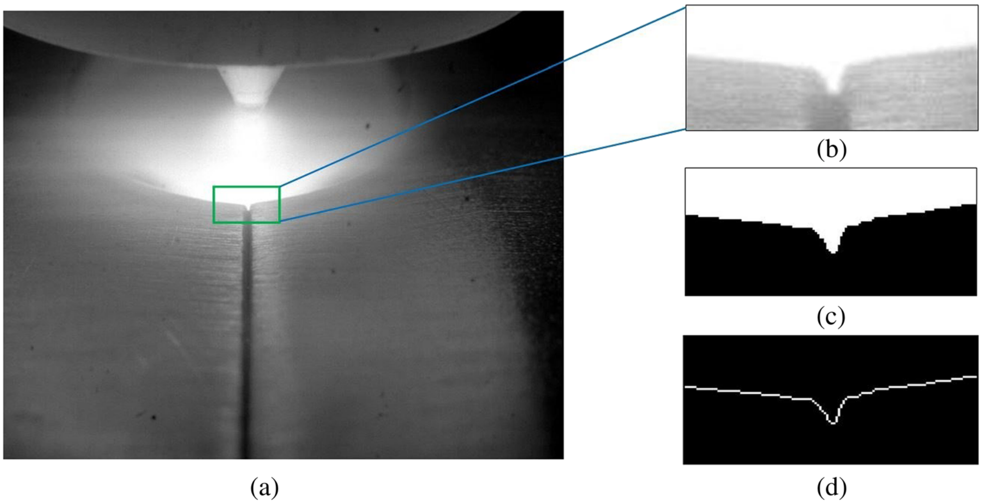

Fig. 15 Welding-seam identification and processing: **a** welding image; **b** extraction of the weld pool and the weld area; **c** threshold segmentation; **d** edge feature extraction

all the pixels are weighted based on the magnitude of the amplitude and then divided into nine sections, that is, nine features. The feature vectors of all cells in the block are connected to obtain the HOG feature of the block. Finally, the gradient histograms for all cells are formed as 3780 dimensional high-dimensional descriptors-vectors. These vectors are used as the features of windows and are put into SVM for training and classifying. After testing, this method can make the detection accuracy of the window reach 93.2%. However, in a single-weld image, only a small number of windows can be successfully detected, which means one or two wrongly detected windows have a greater influence on the position of ROI2 (as shown in Fig. 14a, b).

Local binary pattern (LBP) has significant advantages, such as rotation invariance and grayscale invariance. The detection window is divided into 32 × 32 cells. For each pixel, the gray values of the adjacent 8 pixels are compared with said pixel and marked as 1 and 0, respectively. The resulting 8-bit binary number is used as the LBP value for this pixel. Then, the frequency histogram for each number in the cell is calculated [23]. The statistical histogram of each cell is connected as a feature vector, which is the LBP texture feature vector of the entire map (as shown in Fig. 13). These vectors are put into SVM for training and classifying. The result of the testing shows that compared with the HOG algorithm, the LBP algorithm can detect more windows, but the detection accuracy rate is reduced to 82.4% (as shown in Fig. 14c, d).

From the above test results, it can be seen that the HOG algorithm has a narrow detection range, and the target windows can be detected with a high accuracy. However, some of them will be missed. The LBP algorithm has a wider detection range, and more windows can be detected, but window misdetection still exists. In this study, the HOG+LBP algorithm is used to obtain the comprehensive features. First, the coordinate center of the windows detected by HOG is obtained. Then, among the windows obtained by LBP, the windows that are more than 100 pixels away from this coordinate center are removed. Finally, the remaining windows extracted by LBP are combined with the windows extracted by HOG. As shown in Fig. 14e, f, ROI2 can be extracted more precisely. Moreover, the target windows can be extracted by the HOG+LBP algorithm with higher accuracy as shown in Table 1.

5.3 Identification of weld characteristics

Since the SVM algorithm has identifies the weld seam area, and the gray value of the weld seam is lower than that of the surrounding area, the coordinates of the middle line of the weld seam can be obtained using the traditional edge detection algorithm. The weld-seam image in Fig. 12b is selected as an example for the following image process, i.e., the single-pixel weld-seam edge is obtained after filtering, threshold segmentation, and the application of the canny algorithm without pseudo-edges or external connectivity areas (as shown in Fig. 15). During the butt-welding process, although the gap width of the base metal is small (less than 0.5 mm), some of the molten metal fills into the seam, so the grayscale of a small section of the seam is almost the same as the weld pool. Therefore, the edges of the area are extracted by image segmentation and an edge detection algorithm.

The edge features are symmetrically distributed on the left and right sides of the seam and mutated in the middle.

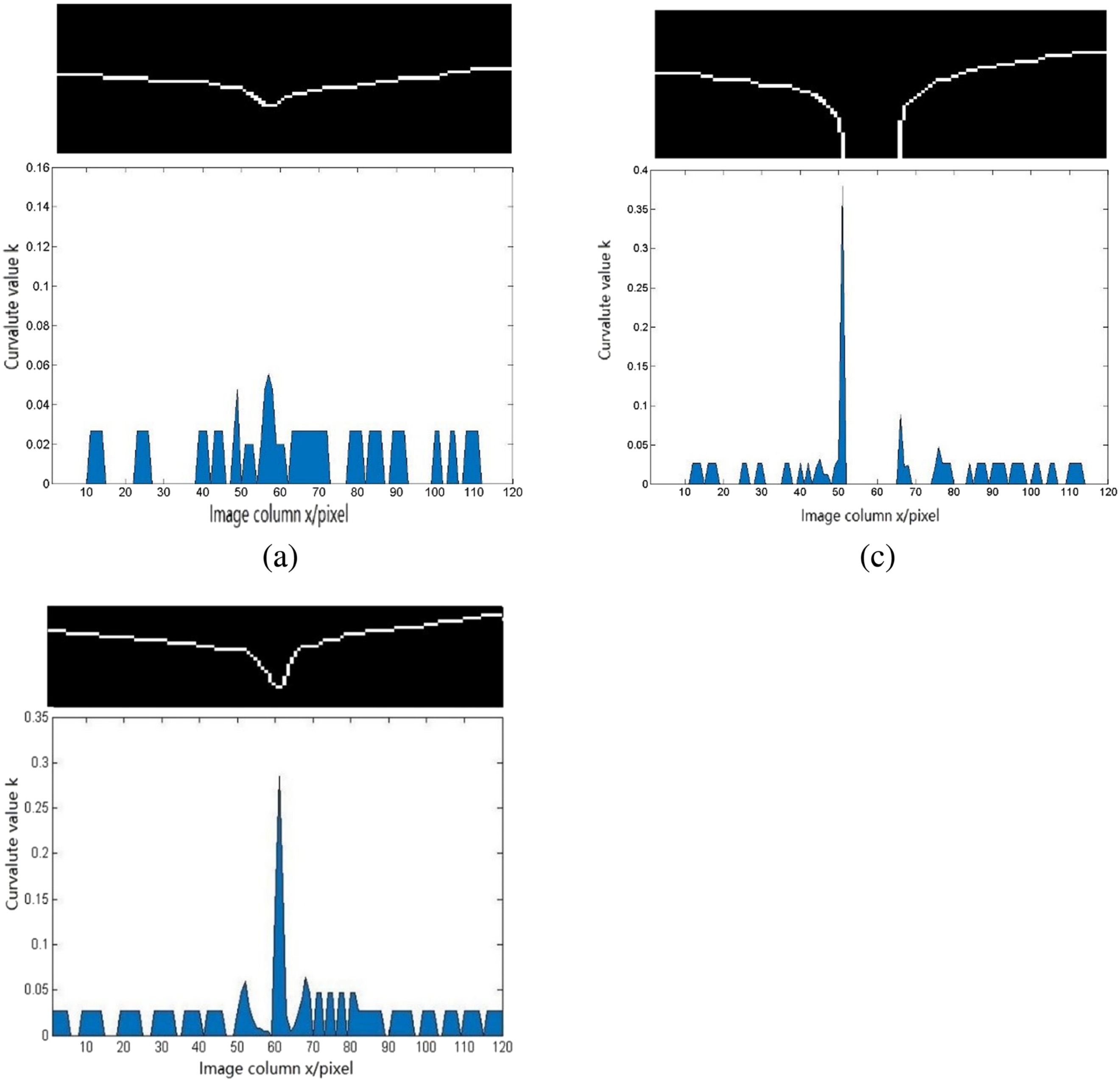

(a)

(c)

(b)

Fig. 16 Welding process curvature evaluation: **a** curvature value for Fig. 12a; **b** curvature value for Fig. 12b; **c** curvature value for Fig. 12c

Therefore, a method based on the contour curvature evaluation is proposed. The edge obtained by the canny algorithm consists of a single layer of discrete pixels. The coordinates of the pixels are extracted and the approximate curvature of each discrete pixel is calculated. The method for calculating the curvature approximation is called the three-point method, which uses the coordinates of three pixels adjacent to the contour to approximate the curvature value [24]. m pixel coordinate points Q_1, $Q_2 \ldots Q_i \ldots Q_m$ are found on the contour, where the coordinate of Q_i is expressed as (x_i, y_i).The curvature equation can be expressed as follows:

$$k_i = \frac{\left| y_i^{\prime\prime} x_i^{\prime} - x_i^{\prime\prime} y_i^{\prime} \right|}{\left| \left(y_i^{\prime 2} + x_i^{\prime 2} \right)^{3/2} \right|} \tag{7}$$

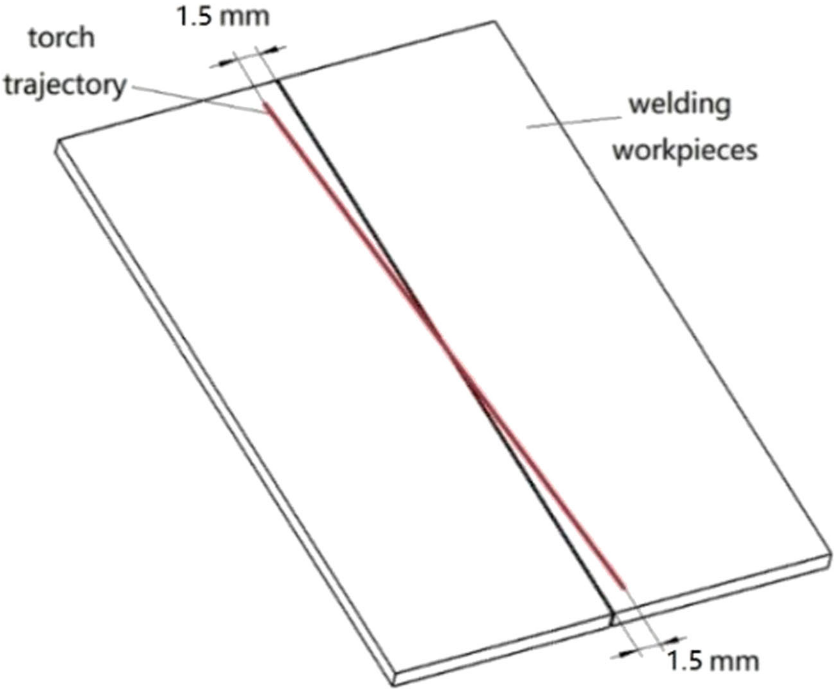

Fig. 17 Sketch map of the torch trajectory

$$\begin{cases} x'_i = x_{i+n} - x_{i-n} \\ x''_i = x_{i+n} + x_{i-n} = 2x_i \\ y'_i = y_{i+n} - y_{i-n} \\ y''_i = y_{i+n} + y_{i-n} - 2y_i \end{cases} \tag{8}$$

where $n = 1, 2 \ldots m$. In this experiment, $n = 3$, which means the curvature is calculated every three points. In the three situations shown in Fig. 12, curvature evaluation method is tested (as shown in Fig. 16). The point where the curvature is the greatest can be considered as the position of the weld. In summary, the curvature evaluation method can effectively detect the weld-seam position, although the position of the seam changes. Therefore, the pixel coordinates of the weld-seam point can be obtained.

6 Experiment and analysis

A series of experiments were conducted in order to verify the accuracy of the deviation-detection algorithm proposed in this paper. In this experiment, 8-mm thick 304 stainless steel plates are selected as the experimental weldment, and a K-TIG deep-penetration welding system is used for welding with the welding current of 500 A. Under the control of the KUKA robot, the torch moves linearly along a preset trajectory. The trajectory is deliberately designed as a diagonal line, which cause the trajectory to not coincide with the weld, but instead intersect with the weld (as shown in Fig. 17).

In the *X*-direction, the starting point of the trajectory deviates from the seam by 1.5 mm while the end point deviates from the seam by − 1.5 mm. When the welding process starts, the HDR camera is used to shoot the welding area and collect images. One single image is extracted from every three frames in the collected video stream, and δ is obtained by the algorithm proposed in this paper. δ is the deviation between the arc centerline and the seam. There are three typical situations during the welding process: torch on the left side of the seam, torch coinciding with the seam, and torch on the right side of the seam. Three welding images are selected that correspond to these situations, and each δ is extracted (as shown in Fig. 18).

During the K-TIG deep-penetration welding process, the relative position between the torch, the camera, and the plane where the workpiece is located does not change. Therefore, the scene observed by the camera is almost unchanged. In addition, the camera's field of view is very narrow, so the lens distortion has little effect on the image. Therefore, the conversion relationship between image coordinates and actual coordinates can be approximated. Through the experimental test, the horizontal correspondence near the pool can be confirmed

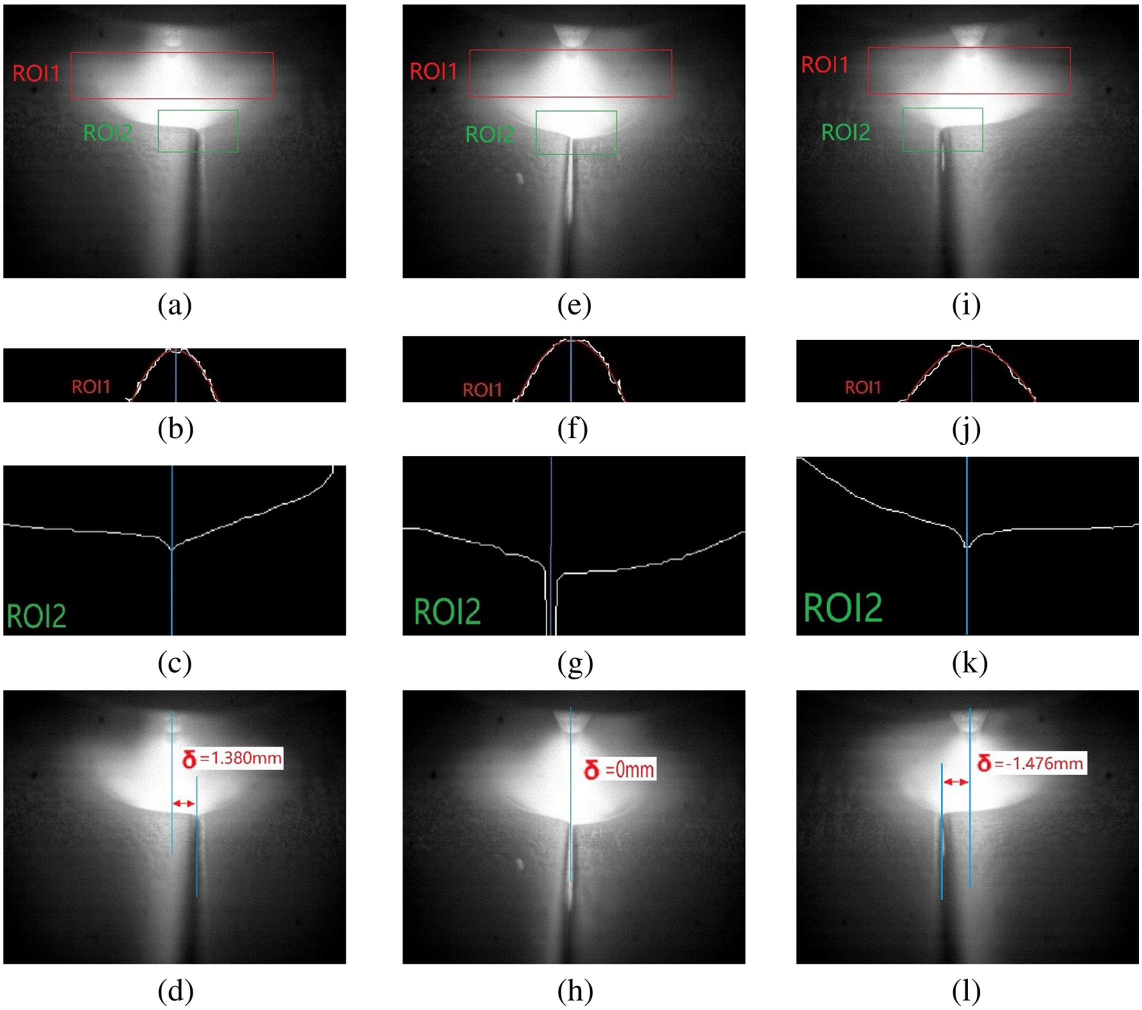

(a) (e) (i) (b) (f) (j) (c) (g) (k) (d) (h) (l)

Fig. 18 Detection of δ in different situations: **a–d** the torch is on the left side of the seam; **e–h** the torch coincides with the seam; **i–l** the torch is on the right side of the seam

to be 0.023 mm/pixel, which can be used to convert the detected deviation from the image coordinate system to the world coordinate system. After the experiment, 250 different δ values are detected, and a comparison chart of the detected deviation (δ) and the actual deviation (δ_0) is shown in Fig. 19.

Defining the measurement error as $\varepsilon = \delta_0 - \delta$. It can be seen from Fig. 20 that the total welding distance is 250 mm and in the first 20 mm, and the deviation measurement value oscillates around the actual value with a large variation range. At some moments, the measurement error exceeds 0.1 mm. As the welding continues, the variation range of the deviation measurement value decreases and the error value is within 0.1 mm. The analysis shows that the high-frequency arcing used in K-TIG welding affects the camera and distorts the image at the moment of arcing. In addition, after arcing, the arc and molten pool have not yet reached a stable state, so there is a relatively large error in the measurement of the deviation at the beginning of the welding. On the whole, the average of ε is 0.0303 mm and the deviation detection process is stable, so the proposed algorithm generally has a high degree of accuracy in detecting the welding deviation during the K-TIG deep penetration welding process.

7 Conclusion

During the K-TIG deep-penetration welding process, the arc is intense and the seam is narrow. In this case, a welding-deviation-detection method is proposed to realize seam tracking in K-TIG deep-penetration welding process. The main conclusions are drawn as follows:

1. The noise in the original image is determined as Gaussian noise via noise analysis, which is the basis for further image denoising using bilateral filtering.

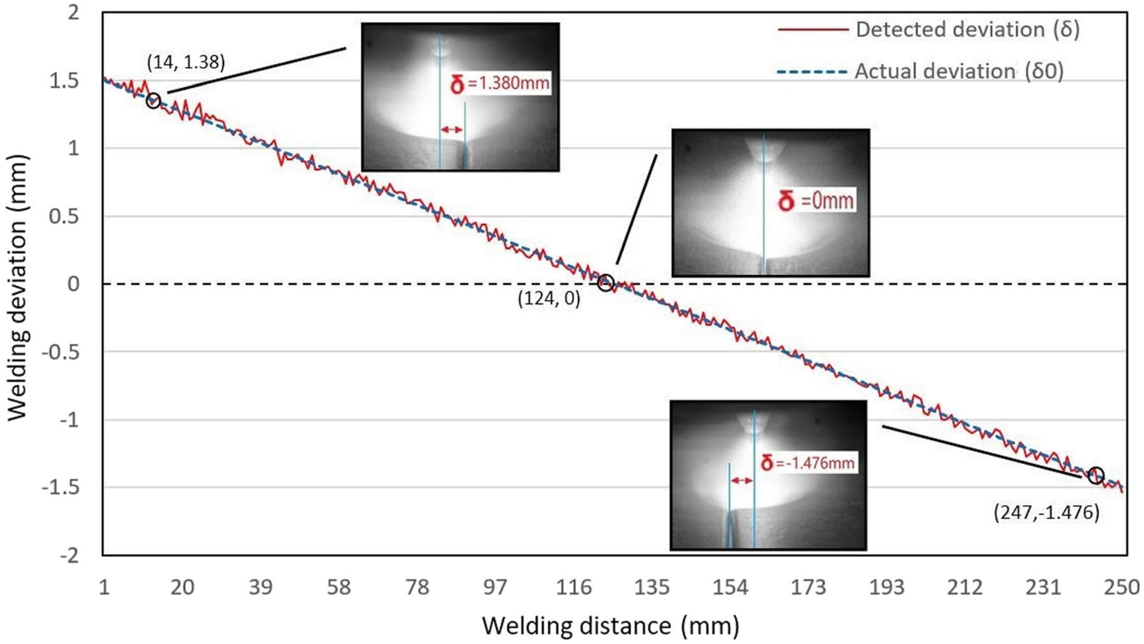

Fig. 19 Comparison between detected deviations and actual deviations

2. The extraction of the deviation between the arc centerline and the weld seam depends on two novel image processing algorithms, i.e., an improved Otsu algorithm which achieves a better binarization effect to extract the arc centerline and an adaptive area algorithm which extracts the ROI and obtains the position of the weld seam.
3. The accuracy of the proposed method has been verified through experimentation and the average accuracy of error detection is within ± 0.04 mm.

The proposed method provides a solution to the detection of welding details under a strong arc light, as well as the

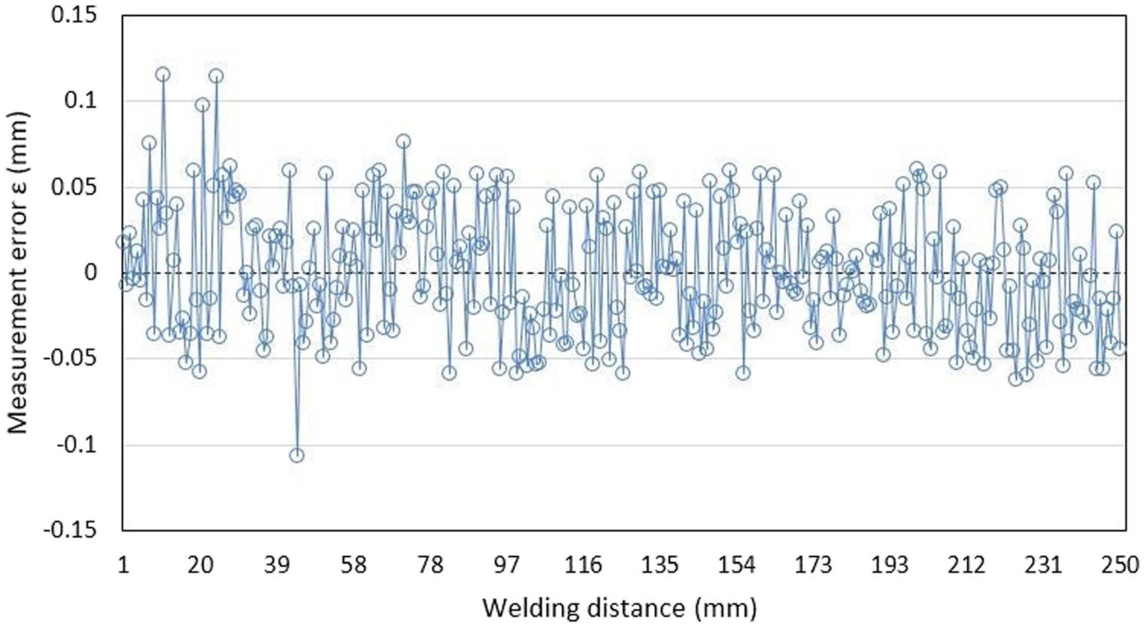

Fig. 20 Measurement error during the test

detection of a narrow gap seam. It has an application value for weld-seam tracking in high current welding and narrow-seam welding.

Funding information This study is financially supported from the Science and Technology Planning Project of Guangdong Province (grant no. 2015B010919005) and the Science and Technology Planning Project of Guangzhou City (grant no. 201604046026, 201510010230).

References

1. Zhang YM, Kovacevic R (1997) Real-time sensing of sag geometry during GTA welding. J Manuf Sci E-T ASME 119(2):151–160
2. Zhang YM, Kovacevic R (1998) Neurofuzzy model-based predictive control of weld fusion zone geometry. IEEE T Fuzzy Syst 6(3): 389–401
3. Kiddee P, Fang ZJ, Tan M (2016) An automated weld seam tracking system for thick plate using cross mark structured light. Int J Adv Manuf Technol 87(9–12):3589–3603
4. Ding Y, Huang W, Kovacevic R (2016) An on-line shape-matching weld seam tracking system. Robot Cim-Int Manuf 42:103–112
5. Wang XJ, Shi YH, Yu GQ, Liang B, Li Y (2016) Groove-center detection in gas metal arc welding using a template-matching method. Int J Adv Manuf Technol 86(9–12):2791–2801
6. Shen HY, Wu J, Lin T, Chen SB (2008) Arc welding robot system with seam tracking and weld pool control based on passive vision. Int J Adv Manuf Technol 39:669–678
7. Ye Z, Fang G, Chen S, Zou JJ (2013) Passive vision based seam tracking system for pulse-mag welding. Int J Adv Manuf Technol 67(9–12):1987–1996
8. GAO X, Chen Y (2014) Detection of micro gap weld using magneto-optical imaging during laser welding. Int J Adv Manuf Technol 73(1–4):23–33
9. Yang CL, Guo N, Lin SB, Fan CL, Zhang YQ (2009) Application of rotating arc system to horizontal narrow gap welding. Sci Technol Weld Joi 14(2):172–177
10. Cui S, Shi Y, Sun K, Gu S (2018) Microstructure evolution and mechanical properties of keyhole deep penetration TIG welds of S32101 duplex stainless steel. Mat Sci Eng A-Struct 709:214–222
11. Ge J, Zhu Z, He D, Chen L (2005) A vision-based algorithm for seam detection in a PAW process for large-diameter stainless steel pipes. Int J Adv Manuf Technol 26(10):1006–1011
12. Larson GW, Rushmeier H, Piatko C (1997) A visibility matching tone reproduction operator for high dynamic range scenes. IEEE T Vis Comput Gr 3(4):291–306
13. GAO J, Qin G, Yang J, He J, Zhang T, WU C (2011) Image processing of weld pool and keyhole in Nd:YAG laser welding of stainless steel based on visual sensing. T Nonferr Metal Soc 21(2):423–428
14. Xu Y, Fang G, Lv N, Chen S, Zou JJ (2015) Computer vision technology for seam tracking in robotic GTAW and GMAW. Robot Cim-Int Manuf 32(C):25–36
15. Chang SG, Yu B, Vetterli M (2000) Spatially adaptive wavelet thresholding with context modeling for image denoising. IEEE T Image Process 9(9):1522–1531
16. Zhang M, Gunturk BK (2008) Bilateral filtering for gray and color images. IEEE T Image Process 17(15):2324–2333
17. Otsu N (1979) A threshold selection method from gray-level histograms. IEEE T Syst Man Cy B 9(1):62–66
18. Fitzgibbon A, Pilu M, Fisher RB (1995) Direct least square fitting of ellipses. IEEE T Pattern Anal 21(5):476–480
19. Kim SJ, Koh K, Lustig M, Boyd S, Gorinevsky D (2008) An interior-point method for largescale l1-regularized least squares. IEEE J Sel Top Quant 1(4):606–617
20. Xu Y, Yu G, Wang Y, Wu X, Ma Y (2016) A hybrid vehicle detection method based on Viola-Jones and HOG + SVM from UAV images. Sensors-Basel 16(8):1325
21. Cao X, Wu C, Yan P, Li X (2011) Linear SVM classification using boosting HOG features for vehicle detection in low-altitude airborne videos. Image Processing (ICIP), 18th IEEE International Conference on pp. 2421–2424
22. Llorca DF, Arroyo R, Sotelo MA (2014) Vehicle logo recognition in traffic images using HOG features and SVM. International IEEE Conference on Intelligent Transportation Systems
23. Pujol FA, Jimeno-Morenilla A, Sanchez-Romero JL (2017) Face recognition using a hybrid SVM-LBP approach and the Indian movie face database. Curr Sci India accepted 5:974–977
24. Zou Y, Jiang LP, LI YH, Xue L, Huang JF, Huang JQ (2016) Welding deviation detection algorithm based on extremum of molten pool image contour. Chin J Mech Eng-En 29(1):74–83